Available online at www.sciencedirect.com
SCIENCE DIRECT®
International Journal of Multiphase Flow 30 (2004) 27–50
International Journal of Multiphase Flow
www.elsevier.com/locate/ijmulflow

Preferential concentration of particles in a fully developed turbulent square duct flow

C.M. Winkler [a], Sarma L. Rani [b], S.P. Vanka [c,*]

[a] *The Boeing Company, P.O. Box 516, St. Louis, MO 63166, USA*
[b] *Sibley School of Mechanical and Aerospace Engineering, Upson Hall, Cornell University, Ithaca, NY 14853, USA*
[c] *Department of Mechanical and Industrial Engineering, University of Illinois at Urbana-Champaign, 1206 W. Green St., Urbana, IL 61801, USA*

Received 2 June 2002; received in revised form 22 October 2003

Abstract

The preferential concentration of dense particles in a downward, fully developed turbulent square duct flow at $Re_\tau = 360$, based on mean friction velocity and duct width, is studied using large eddy simulations. Due to the low volume fractions involved (maximum volume fraction $<10^{-5}$), one-way coupled simulations are performed, i.e., two-way coupling and particle–particle collisions are not considered. The continuous and the dispersed phases are treated using Eulerian and Lagrangian approaches, respectively. A finite volume based second-order accurate fractional step scheme is used to integrate the unsteady, three-dimensional Navier–Stokes equations. The subgrid stresses are modeled with a dynamic subgrid kinetic energy model, as reported previously. The particle equation of motion includes drag, lift and gravity forces and is integrated using the fourth-order accurate Runge–Kutta method. Four cross-sectional locations representative of the mean secondary flow patterns and six particle response times were chosen to study the effect of location and particle inertia on preferential concentration.

To demonstrate preferential concentration, variation of vorticity magnitude, swirling strength, maximum compressional strain-rate, and $\nabla\mathbf{u} : \nabla\mathbf{u}$, and their probability distribution functions (PDF) conditioned on particle presence, with particle response time is presented. Since the square duct cross-section is inhomogeneous, we also study variation in preferential concentration with cross-sectional location. Particles are seen to accumulate in regions of high $\nabla\mathbf{u} : \nabla\mathbf{u}$ and strain-rate and in regions of low swirling strength. In general, particles accumulate in regions of low vorticity magnitude. However, near the wall, the tendency of particles to accumulate in regions of high vorticity increases with response time.

Keywords: Square duct; Particles; Large eddy simulation

* Corresponding author.

0301-9322/$ - see front matter © 2003 Elsevier Ltd. All rights reserved.
doi:10.1016/j.ijmultiphaseflow.2003.11.003

1. Introduction

Particle transport in turbulent flows has applications ranging from industrial sprays, electrostatic precipitators, and internal combustion engines to pollutant transport in the atmosphere and oceans. In many of these flows, the primary issues of concern are particle dispersion, deposition and mixing. Particle dispersion involves the transport of particles by the turbulent flow structures. It can be somewhat counterintuitive to think of turbulence as a mechanism which "de-mixes" particles. However, preferential concentration of particles in turbulent flows is known to occur (Squires and Eaton, 1990; Wang and Maxey, 1993; Wang and Squires, 1996). Non-uniform particle and droplet concentrations in flows can significantly inhibit reaction and combustion rates as well as decrease the efficiency of evaporators in heat exchangers. Therefore, it is important to have a fundamental understanding of this phenomenon. Numerical simulations have become a valuable tool for studying preferential concentration as they allow quantities to be computed that are often difficult to measure experimentally. Attempts to predict particle-laden turbulent flows have resulted in several computational techniques which can generally be classified as either Eulerian or Lagrangian. Eulerian approaches envision the dispersed phase as a continuum and, equations governing its momentum and continuity are formulated and solved much like the carrier phase. In the Lagrangian method, trajectories of individual particles are computed by solving the particle equation of motion. A recent review of numerical methods for particle-laden flows is given by Loth (2000).

The classification of the carrier flow simulations can be made according to the degree of resolution of the turbulent flow scales. The most accurate method for simulating turbulence is known as Direct Numerical Simulation (DNS). In DNS, all scales of motion are resolved without any modeling or empiricism. The only errors that arise are from the numerical method used to solve the equations. Although highly accurate, DNS is restricted to relatively low Reynolds numbers, since the computational resources needed to fully resolve high Reynolds number turbulent flows are often prohibitive. A less computationally intensive method is Large Eddy Simulation (LES), which resolves only the large, energy containing scales in the flow and models the effects of the small scales, which are thought to be universal. Modeling of the unresolved, or subgrid scales, has resulted in several works on LES. A recent review of LES models is given by Meneveau and Katz (2000).

There are a number of previous studies on turbulent flow in geometries such as isotropic turbulence (Yeung and Pope, 1989), channels (Kim et al., 1987) and pipes of circular cross-section (Eggels et al., 1994). However, only a few studies on internal flows with only one homogeneous direction, such as a square duct, have been conducted. For unladen flow, one of the first LES studies in a square duct was performed by Madabhushi and Vanka (1991) using the Smagorinsky model and a $65\times65\times32$ grid at $Re_\tau = 360$. They were able to predict the turbulence driven secondary flows using LES. An interesting feature observed was that the instantaneous cross-stream velocities were as high as ten times their time-averaged values. Also, the secondary flows were found to convect mean flow momentum from the center of the duct to its corners. This caused a bulging of the streamwise velocity contours towards the corners. They also noted that the Reynolds normal and shear stresses equally contribute to the production of mean streamwise vorticity. Other studies on single phase flow in a square duct include those of Demuren and Rodi (1984), Kajishima and Miyake (1992), Gavrilakis (1992), Huser and Biringen (1993), Madabhushi

(1993) and Madabhushi and Vanka (1993). In related work, Bradshaw (1987) examined secondary flows in curved ducts.

To the authors' knowledge, no work involving particle transport in square ducts has been reported. However, gas-particle flows in simpler geometries have been studied by a number of researchers (Wang and Maxey, 1993; Wang and Squires, 1996; Uijttewaal and Oliemans, 1996; Zhang and Ahmadi, 2000). It is known that in isotropic turbulence, particles preferentially accumulate in regions of low vorticity and high strain-rate (Squires and Eaton, 1990). Ferry and Balachandar (2001) examined channel flow and showed that fluid statistics such as the swirling strength, λ_i, and maximum compressional strain-rate, σ_u, provide a better indication of the preferential concentration of particles. They demonstrated that particles collect in regions of low λ_i and high σ_u. The swirling strength, which is the magnitude of the imaginary part of the complex conjugate eigenvalue pair of the fluid velocity gradient tensor, has been used to identify vortices (Zhou et al., 1998; Adrian et al., 2001). The swirling strength is zero when all the eigenvalues of $\nabla\mathbf{u}$ are all real. A positive value of λ_i corresponds to a local dominance of rotation-rate over strain-rate (Adrian et al., 2001).

Vorticity can arise from either swirling or shear. However, it is the swirl that has a greater centrifugal effect on particles than shear and hence is a better choice than vorticity for preferential concentration studies. The maximum compression strain-rate, σ_u, is the most negative eigenvalue of the strain-rate tensor. Other quantities which are useful in identifying regions of preferential concentration of particles include $\nabla\mathbf{u} : \nabla\mathbf{u}$ and enstrophy (Druzhinin and Elghobashi, 1998).

To fully appreciate the significance of $\nabla\mathbf{u} : \nabla\mathbf{u}$, one must examine its derivation. Consider an Eulerian formulation for the particle velocity field. To first order in particle response time τ_p, if one neglects body forces, the particle velocity field, $\mathbf{u}_p$, may be expressed as a function of the fluid velocity field, $\mathbf{u}$, and particle response time, τ_p, as follows (Maxey, 1987; Ferry and Balachandar, 2001)

$$\mathbf{u}_p = \mathbf{u} - \tau_p\left(\frac{\partial \mathbf{u}}{\partial t} + \mathbf{u}\cdot\nabla\mathbf{u}\right) \tag{1}$$

Maxey (1987) has shown that this particle velocity field is not divergence free. Taking the divergence of (1) gives

$$\nabla\cdot\mathbf{u}_p = -\tau_p\frac{\partial u_j}{\partial x_i}\frac{\partial u_i}{\partial x_j} = -\tau_p\nabla\mathbf{u} : \nabla\mathbf{u} \tag{2}$$

It is clear from (2) that particles will accumulate where $\nabla\mathbf{u} : \nabla\mathbf{u}$ is positive.

Fessler et al. (1994) also studied preferential concentration of particles in channel flow. Fessler et al. (1994) experimentally found that when the Stokes number (based on the Kolmogorov time scale) was approximately one, the particles had the maximum departure from a random distribution. Zhang and Ahmadi (2000) examined the deposition of particles in a channel flow. In their work, particles are seen to deposit along low speed streaks which suggests that particles are neither uniformly nor randomly dispersed in the flow field. In geometries with two homogeneous directions, such as channels and pipes, the preferential concentration statistics vary in only one direction. In isotropic turbulence, statistics are not a function of any direction. However, in a square duct, the secondary flows in the cross-section, resulting from gradients in the Reynolds stresses, add additional complexity to the preferential concentration phenomenon.

Other researchers, such as Chung and Troutt (1988), who studied a particle-laden axisymmetric jet, have suggested that there exists a range of the particle response time where the particles may undergo preferential concentration. They state that particles with large response times are dispersed the least.

Crowe et al. (1995) have observed that in the wake of a bluff body, particles tend to accumulate along the edges of vortex structures. They term this phenomenon "focusing", analogous to the preferential concentration. Particles with a Stokes number (St) of unity are found to exhibit the maximum focusing. However, they only studied Stokes numbers of 0.01, 1.0, and 100, which does not accurately resolve the trend around $St = 1$, where the focusing effect is maximum.

In a mixing layer, Tageldin and Cetegen (1997) experimentally observed size-selective dispersion of droplets. They found rapid entrainment of small droplets and found a much slower entrainment of large droplets due to Stokes number effects. This confirms the findings of Lazaro and Lasheras (1992a,b), who also mention that the particle concentration field is related to the streaky nature of the large-scale structures. Further experimental evidence of non-uniform particle dispersion is given in Longmire and Eaton (1992), who studied a particle-laden round jet. They suggest that convection from large-scale turbulent structures controls local particle concentration and dispersion.

Despite the relatively large number of works on preferential concentration of particles in turbulence, there is a lack of information on this phenomenon in complex turbulent flows. In the present study, particle-laden turbulent flow in a square duct is investigated. It is expected that the secondary flows in a square duct will provide additional complexities compared to a channel flow, and the particle dispersion may be significantly enhanced as a result of the strong secondary flows. Several particle response times and cross-sectional locations in the square duct are studied to identify the statistical trends of the effects of secondary flows on preferential concentration of particles.

2. Overview of the simulations

2.1. Numerical method

The incompressible form of the three-dimensional, unsteady Navier–Stokes equations is solved using a second-order accurate finite volume method with central differencing of spatial derivatives on a non-staggered grid. The friction Reynolds number based on average friction velocity, $u_\tau = (\bar{\tau}_w/\rho_f)^{1/2}$, and duct width, δ, is $Re_\tau = 360$, where $\bar{\tau}_w$ and ρ_f are the mean wall shear stress averaged over the four walls and the fluid density, respectively. Diffusion terms are handled with the Crank–Nicholson scheme and the convective terms with the second-order accurate Adams–Bashforth scheme. The Harlow–Welch fractional step method was used to decouple the momentum and continuity equations. An algebraic multigrid solver was used to solve the pressure Poisson equation resulting from the fractional step method. The equations of motion for the fluid are given by

$$\nabla \cdot \mathbf{u} = 0 \tag{3}$$

$$\frac{\partial \mathbf{u}}{\partial t} + \nabla \cdot (\mathbf{uu}) = -\nabla p + \frac{1}{Re_\tau}\nabla^2 \mathbf{u} \tag{4}$$

where the quantities have been made dimensionless by u_τ and δ. The time scale is given by δ/u_τ. The square duct dimensions are $\delta \times \delta \times 2\pi\delta$ and the grid consisted of $80\times80\times128$ unstructured Cartesian cells, in the respective directions. The components of the velocity vector $\mathbf{u}$ in the two wall-normal and streamwise directions are u, v and w, respectively. The dimensionless time step is set to 1×10^{-4}. This time step is smaller than the smallest particle response time and hence sufficient to resolve the particle trajectories.

Top-hat filtering, implemented through finite-volume implicit grid-filtering, was used to generate the equations governing the transport of the large eddies. After filtering, the equations of motion become the following

$$\nabla \cdot \bar{\mathbf{u}} = 0 \tag{5}$$

$$\frac{\partial \bar{u}_i}{\partial t} + \frac{\partial}{\partial x_j}(\bar{u}_i \bar{u}_j) = -\frac{\partial \bar{P}}{\partial x_i} + \frac{\partial}{\partial x_j}\left[\left(\frac{1}{Re_\tau} + \nu_\mathrm{T}\right)\frac{\partial \bar{u}_i}{\partial x_j}\right] + \frac{\partial}{\partial x_j}\left(\nu_\mathrm{T}\frac{\partial \bar{u}_j}{\partial x_i}\right) + 4\delta_{i3} \tag{6}$$

The "over-bar" notation denotes application of the top-hat filter. The last term on the right hand side of (6) represents the mean streamwise pressure gradient. The eddy viscosity, ν_T, is determined from the subgrid kinetic energy, as described in the following section.

2.2. Subgrid modeling

The subgrid scales are modeled with a dynamic subgrid kinetic energy model developed by Kim and Menon (1997). The test-filter grid, having a resolution of $40\times40\times64$ in the two wall normal (x and y) and streamwise (z) directions, respectively, was first generated. A 2.5% geometric progression grid stretching is used on the test filter grid in the wall normal directions. Each test-filter grid cell was then subdivided into 8 uniform fine-grid cells, which gave a final grid resolution of $80\times80\times128$. The first node away from the wall was located at 1.76 wall units.

The dynamic subgrid kinetic energy model employed in this work, given in detail in Kim and Menon (1997), can be summarized as follows. The transport equation for the subgrid kinetic energy, k_sgs, is given as

$$\frac{\partial k_\mathrm{sgs}}{\partial t} + \bar{u}_i \frac{\partial k_\mathrm{sgs}}{\partial x_i} = \nu_\mathrm{T}|\bar{\mathbf{S}}|^2 - \varepsilon + \frac{\partial}{\partial x_i}\left(\nu_\mathrm{T}\frac{\partial k_\mathrm{sgs}}{\partial x_i}\right) \tag{7}$$

where the eddy viscosity, ν_T, is given by

$$\nu_\mathrm{T} = C_t \bar{\Delta} k_\mathrm{sgs}^{1/2} \tag{8}$$

and the dissipation rate, ε, is given by

$$\varepsilon = C_e \frac{k_\mathrm{sgs}^{3/2}}{\bar{\Delta}} \tag{9}$$

where $\bar{\Delta}$ is the grid scale and C_e and C_t are dynamically determined. The resolved strain-rate tensor, $\bar{\mathbf{S}}$, is expressed as

$$\bar{S}_{ij} = \frac{1}{2}\left(\frac{\partial \bar{u}_i}{\partial x_j} + \frac{\partial \bar{u}_j}{\partial x_i}\right) \tag{10}$$

and its magnitude is defined as

$$|\bar{\mathbf{S}}| = \sqrt{2\bar{S}_{ij}\bar{S}_{ij}} \tag{11}$$

Let the "hat" notation symbolize the application of the test filter to a quantity and the "overbar" notation symbolize application of the grid filter. The Leonard stress tensor is then defined as

$$L_{ij} = \widehat{\bar{u}_i\bar{u}_j} - \hat{\bar{u}}_i\hat{\bar{u}}_j \tag{12}$$

The kinetic energy at the test filter level can be found from the trace of (12)

$$k_{\text{test}} = \frac{1}{2}\left(\widehat{\bar{u}_k\bar{u}_k} - \hat{\bar{u}}_k\hat{\bar{u}}_k\right) \tag{13}$$

The dissipation at the test filter level is expressed as

$$\varepsilon_{\text{test}} = (\nu + \nu_{\text{T}})\left(\widehat{\frac{\partial \bar{u}_i}{\partial x_j}\frac{\partial \bar{u}_i}{\partial x_j}} - \frac{\partial \hat{\bar{u}}_i}{\partial x_j}\frac{\partial \hat{\bar{u}}_i}{\partial x_j}\right) \tag{14}$$

Through a similarity assumption between the subgrid stress tensor and the Leonard stress tensor, one can arrive at the following equation

$$L_{ij} = -2C_t\hat{\Delta}k_{\text{test}}^{1/2}\hat{\bar{S}}_{ij} + \frac{1}{3}\delta_{ij}L_{\text{kk}} \tag{15}$$

The least-square method of Lilly (1992) is then used to obtain a formula for C_t

$$C_t = \frac{1}{2}\frac{L_{ij}\sigma_{ij}}{\sigma_{ij}\sigma_{ij}} \tag{16}$$

where

$$\sigma_{ij} = -\hat{\Delta}k_{\text{test}}^{1/2}\hat{\bar{S}}_{ij} \tag{17}$$

By invoking a similarity assumption between the dissipation at the test filter and grid filter levels, an equation for the dissipation at the test filter level is given as

$$\varepsilon_{\text{test}} = C_e\frac{k_{\text{test}}^{3/2}}{\hat{\Delta}} \tag{18}$$

One may now calculate C_t and C_e. These constants have been constrained to be positive in the current simulations.

2.3. Particle motion

The particle equation of motion includes drag, lift in the two wall directions (x and y) and gravity in the streamwise direction (z) and is given by Eq. (19):

$$m_{\mathrm{p}}\frac{\mathrm{d}\mathbf{u}_{\mathrm{p}}}{\mathrm{d}t}=m_{\mathrm{p}}\frac{(\mathbf{u}(\mathbf{x}_{\mathrm{p}})-\mathbf{u}_{\mathrm{p}})}{\tau_{\mathrm{p}}}+(m_{\mathrm{p}}-m_{\mathrm{f}})\mathbf{g}+3.08m_{\mathrm{p}}\frac{\nu^{1/2}}{d_{\mathrm{p}}\frac{\rho_{\mathrm{p}}}{\rho_{\mathrm{f}}}}(w-w_{\mathrm{p}})\left|\frac{\partial w}{\partial x}\right|^{1/2}\mathrm{sgn}\left(\frac{\partial w}{\partial x}\right)\delta_{i1}$$
$$+3.08m_{\mathrm{p}}\frac{\nu^{1/2}}{d_{\mathrm{p}}\frac{\rho_{\mathrm{p}}}{\rho_{\mathrm{f}}}}(w-w_{\mathrm{p}})\left|\frac{\partial w}{\partial y}\right|^{1/2}\mathrm{sgn}\left(\frac{\partial w}{\partial y}\right)\delta_{i2}, \tag{19}$$

where $\mathbf{u}_{\mathrm{p}}$ is the particle velocity vector with w_{p} being its streamwise component, m_{p} and m_{f} are the particle and fluid mass, respectively, $\mathbf{g}$ is gravitational acceleration, d_{p} is the particle diameter, ρ_{p} and ρ_{f} are the particle and fluid densities, respectively, and ν is the kinematic viscosity. The notation "sgn" implies taking the sign of the bracketed quantity. The particle response time is given as

$$\tau_{\mathrm{p}}=\frac{4d_{\mathrm{p}}\rho_{\mathrm{p}}}{3C_{\mathrm{d}}\rho_{\mathrm{f}}|\mathbf{u}(\mathbf{x}_{\mathrm{p}})-\mathbf{u}_{\mathrm{p}}|} \tag{20}$$

where the drag coefficient is taken to be the following:

$$C_{\mathrm{d}}=\left(\frac{24}{Re_{\mathrm{p}}}\right)\left(1+0.15Re_{\mathrm{p}}^{0.687}\right) \tag{21}$$

with the particle Reynolds number defined as

$$Re_{\mathrm{p}}=\frac{|\mathbf{u}(\mathbf{x}_{\mathrm{p}})-\mathbf{u}_{\mathrm{p}}|d_{\mathrm{p}}}{\nu} \tag{22}$$

The particle equation of motion is solved using the fourth-order Runge–Kutta scheme. Six different particle response times are studied in this work, and are given in Table 1 along with corresponding diameters and density ratios. The particle response time, τ_{p}^{+}, is given in wall units. Subgrid fluctuations of $\sqrt{2k_{\mathrm{sgs}}/3}$ are scaled by a Gaussian distributed random number and isotropically added to the fluid velocity at the particle position to more accurately represent the instantaneous velocity. For each different response time, trajectories of 400,000 particles are computed. Elastic collisions with the wall are assumed. The particles are initially positioned randomly in the domain with initial velocities equal to the local fluid velocity and are evolved for at least 10 particle response times (based on the largest τ_{p}) to allow the particles to lose any initial inertial effects. Statistics are then averaged for at least 19 particle response times (and over 604 particle response times for the smallest particles). Statistics were averaged in the homogeneous direction as well as in symmetric planes in the cross-section when appropriate. Since it is only by

Table 1
Particle properties

τ_{p}^{+}	$d_{\mathrm{p}}/\delta\times10^{6}$	$\rho_{\mathrm{p}}/\rho_{\mathrm{f}}$
0.25	117.85	2500
0.5	166.67	2500
1	235.70	2500
2	333.33	2500
4	471.40	2500
8	666.67	2500

chance that a particle is located at a fluid grid point, second order Lagrange polynomials were used to interpolate the fluid quantities to a particle position. This involved 27 fluid quantities (such as u, v, w and k_{sgs}) surrounding the particle.

3. Results

To validate the code, channel flow at $Re_\tau = 180$, based on friction velocity and channel half-height, was simulated on a grid consisting of $100 \times 100 \times 50$ cells in the streamwise, wall-normal, and spanwise directions, respectively. Three LES models were chosen for this validation. The first was the "no-model" LES, which behaves as a coarse grid DNS. The second model chosen was the static coefficient kinetic energy model of Horiuti (1985) with wall-damping. Lastly, the dynamic coefficient kinetic energy model described in Section 2.2 was implemented. Results are compared with the DNS of Kim et al. (1987).

Fig. 1 shows the mean streamwise velocity obtained from each of the various subgrid models. It is seen that the Horiuti model overpredicts the centerline velocity to a greater degree than the other models tested. The no-model LES and the dynamic kinetic energy model give nearly identical results for the streamwise velocity and both compare well with the DNS data.

Fig. 2 displays the streamwise rms velocity given by each of the models. It is seen that the dynamic model most closely matches the DNS data. The Horiuti model and the no-model LES are both seen to overpredict the streamwise rms velocity. But, all models under predict the wall normal rms velocity (Fig. 3). In case of spanwise rms velocity, the no-model LES overpredicts it, while the Horiuti and the dynamic models underpredict it (Fig. 4). Similar trends were observed for the Reynolds stress as well (Fig. 5).

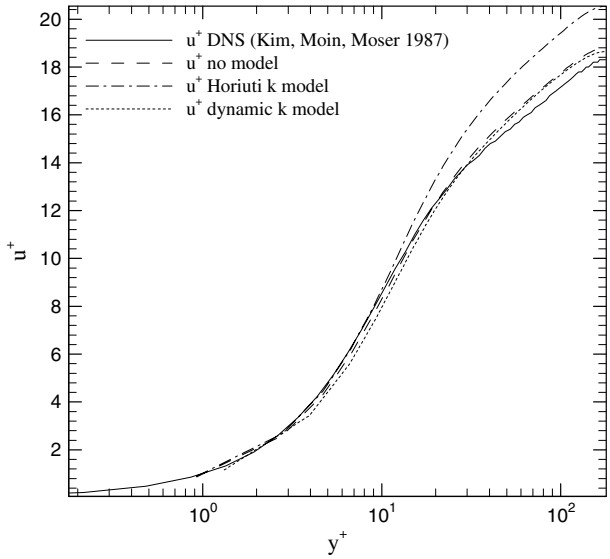

Fig. 1. Mean streamwise velocity for channel flow at $Re_\tau = 180$.

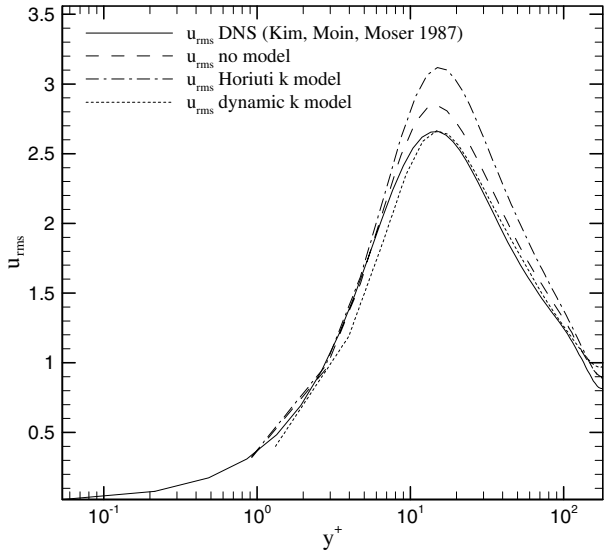

Fig. 2. Mean streamwise RMS velocity for channel flow at $Re_\tau = 180$.

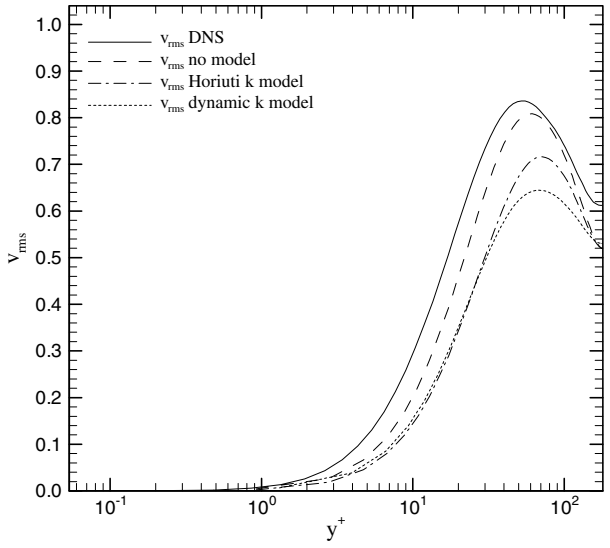

Fig. 3. Mean wall-normal RMS velocity for channel flow at $Re_\tau = 180$.

The LES square duct fluid calculation, using the approach outlined in Section 2.2, was validated against the DNS data of Gavrilakis (1992), who studied the flow at $Re_\tau = 300$. The mean streamwise velocity at the wall bisector is shown in Fig. 6 and agrees within 0.5% at the centerline with Gavrilakis (1992). Fig. 7 displays the rms velocites and it is seen that the peak of the streamwise fluctuating velocity compares within approximately 2% of Gavrilakis (1992) data.

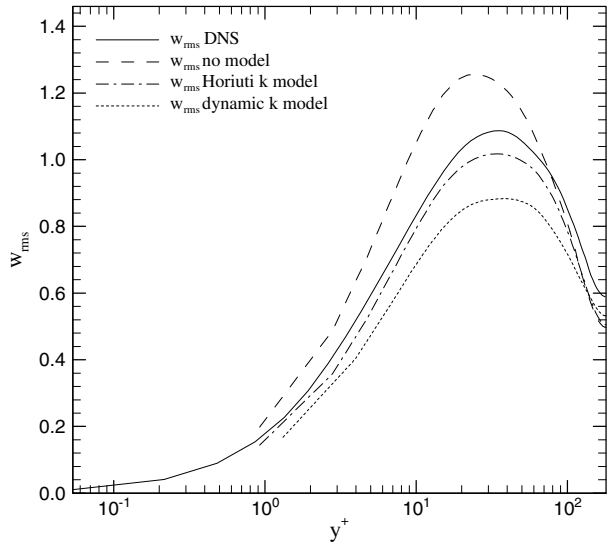

Fig. 4. Mean spanwise RMS velocity for channel flow at $Re_\tau = 180$.

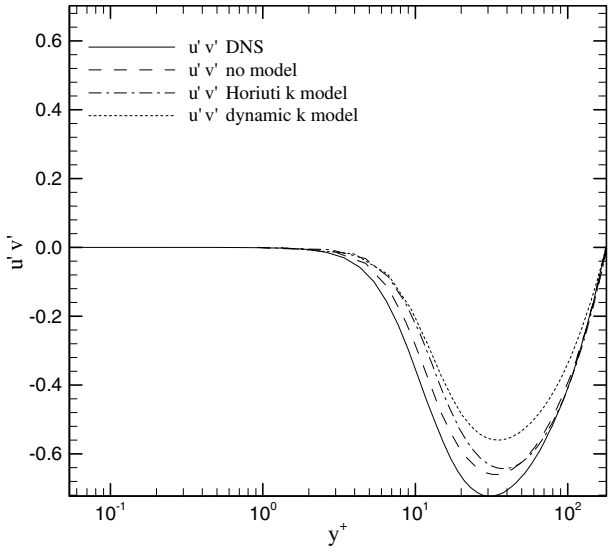

Fig. 5. Mean Reynolds stress for channel flow at $Re_\tau = 180$.

It is pertinent here to briefly consider the qualitative nature of the secondary flows in a square duct. Hence, the cross-sectional contours of the streamwise velocity are shown in Fig. 8. They are in qualitative agreement with those in the above mentioned square duct studies. In the current simulations, the fluid statistics were averaged for more than 60 dimensionless time units.

In the cross-section of a square duct, one may identify different regions of flow patterns. We have chosen four such locations in this work, all identifiable from a time-mean sense (see Fig. 9).

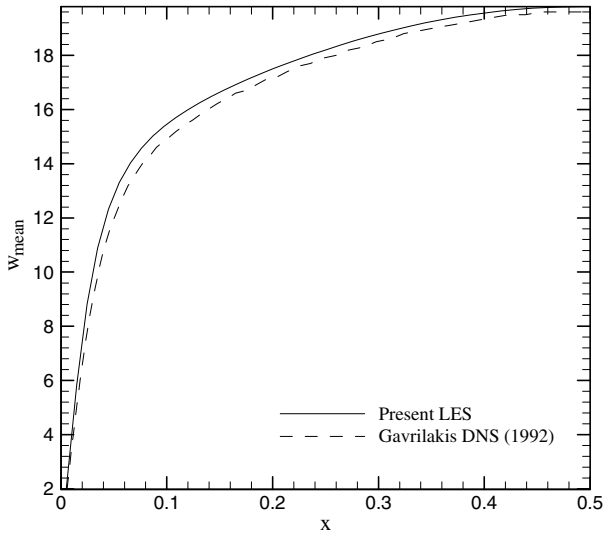

Fig. 6. Mean streamwise velocity at wall bisector.

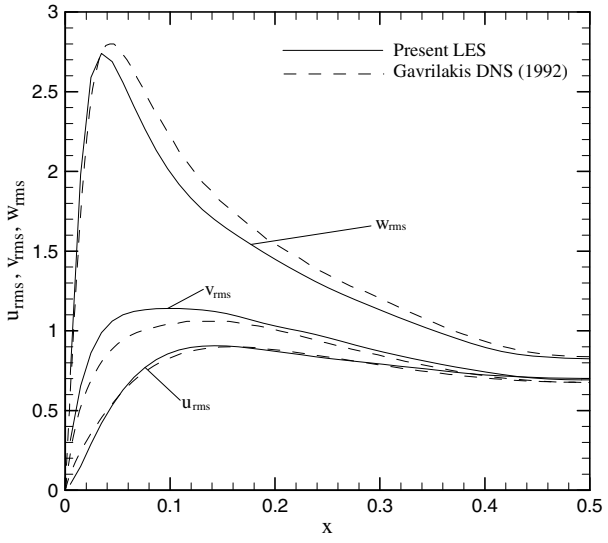

Fig. 7. Mean RMS velocities at wall bisector.

Instantaneously, the eddies are stronger and more complex, as shown in Fig. 10. Due to the finite resolution of the grid, the nearest node to each desired location was chosen. The locations are as follows: the center of the duct where the secondary flows are minimal ($x^+ = 177.2$, $y^+ = 177.2$), the near-wall region ($x^+ = 177.2$, $y^+ = 19.8$), the center of the secondary flow vortices ($x^+ = 76.7$, $y^+ = 31.2$), and the saddle region between the secondary flow vortices ($x^+ = 59.5$, $y^+ = 59.5$). An area of 20.25 square wall units about each point was used to collect particle statistics.

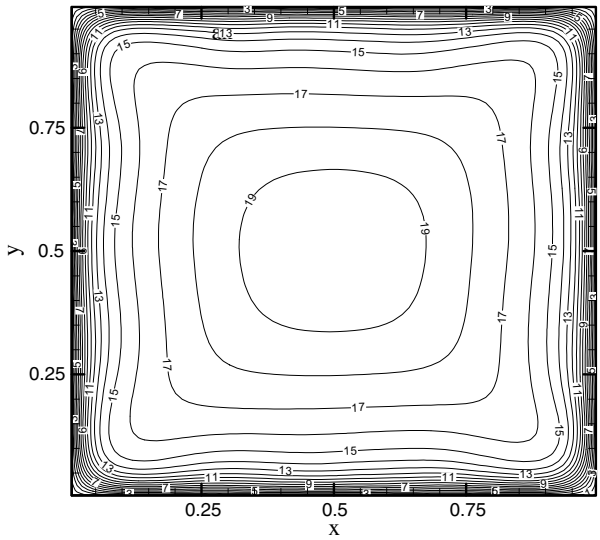

Fig. 8. Mean streamwise velocity contours.

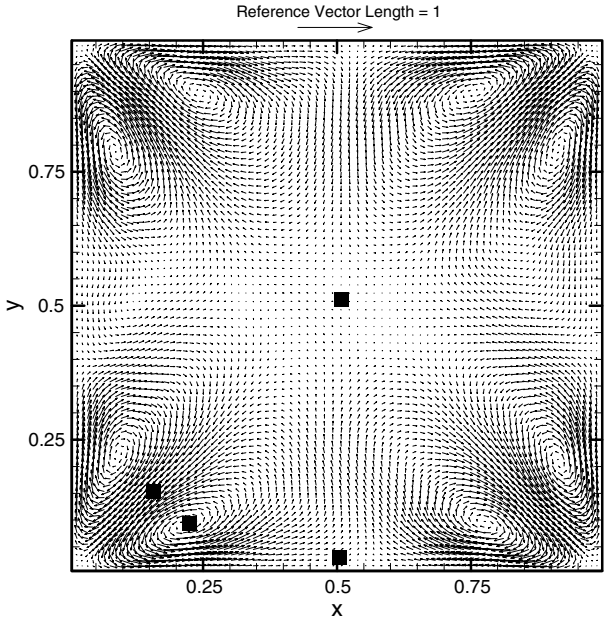

Fig. 9. Mean secondary flows in a square duct shown with four sampling positions.

The subgrid kinetic energy at the wall bisector is shown in Fig. 11. Due to the relatively fine resolution of the grid used in this work, there is little subgrid kinetic energy in the duct center. Thus, the method used to add subgrid fluctuations to the fluid velocity does not significantly alter results in the duct center, i.e., the subgrid energy is not causing a homogenous mixing of particles in the duct center.

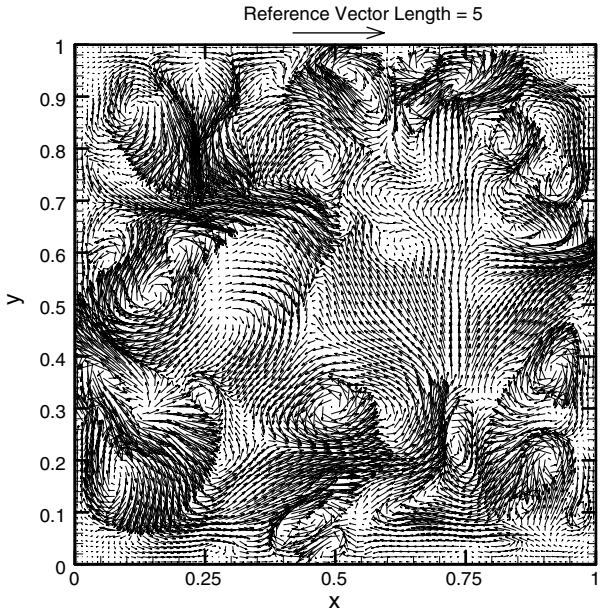

Fig. 10. Instantaneous secondary flows in a square duct.

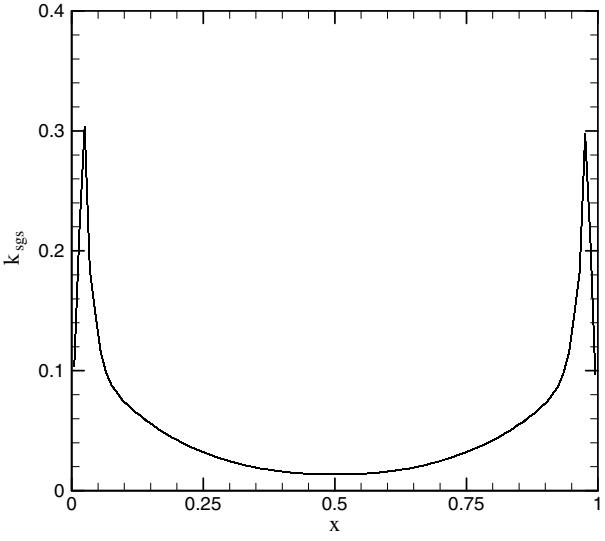

Fig. 11. Subgrid kinetic energy at the wall bisector.

Now, we present variation of $\langle\omega\rangle$, $\langle\lambda_i\rangle$, $\langle\sigma_u\rangle$, and $\langle\nabla\mathbf{u} : \nabla\mathbf{u}\rangle$, and their probability distribution functions, with τ_p^+ and the cross-sectional location. The notation $\langle\ \rangle$ denotes the mean value of a quantity evaluated at the particle locations. It is obtained by interpolating the relevant fluid quantity to the particle positions and then averaging it in the homogeneous direction, time and the

appropriate symmetric cross-sectional points. The corresponding mean values for the fluid (tracer) particles are also presented and are obtained by averaging the grid point values of the fluid quantity in the homogeneous direction, corresponding to the cross-sectional location of interest. The PDFs conditioned on particle presence are averaged only in time and the appropriate symmetric cross-sectional points and are presented for only three values of τ_p^+ ($=0.25$, 1, and 8), along with the corresponding fluid PDF.

3.1. Effect of vorticity magnitude

It has been shown by previous researchers that particles accumulate in regions of low vorticity (Squires and Eaton, 1990; Wang and Maxey, 1993). Typically, when it is stated that particles collect in low vorticity regions, the conclusion is drawn upon evidence from simulations of flows with little or no mean shear, such as isotropic turbulence. However, particles can experience vorticity from either swirl (i.e. rotation) or shear. Consider laminar plane Couette flow. This flow has no large scale swirl, but exhibits vorticity due to the shear. It is vorticity due to swirl that is largely responsible for particles spinning out of vortices and accumulating preferentially. Thus, near walls, where shear plays a dominant role, vorticity is not likely to be a strong measure of preferential concentration. It is for this reason that the swirling strength, $\langle\lambda_i\rangle$, is a better measure of preferential concentration than vorticity. To corroborate this statement, the vorticity magnitude will now be examined to demonstrate that near a wall, where shear dominates, the vorticity (and hence enstrophy) is not a good measure of preferential concentration of particles.

Fig. 12 shows the variation of mean vorticity magnitude $\langle\omega\rangle$, evaluated at the particle positions, with τ_p^+ at the various cross-sectional locations. As expected, the maximum value of $\langle\omega\rangle$, for a given τ_p^+, occurs near the wall. In the near-wall and vortex center regions, as τ_p^+ increases, the particles accumulate in regions of increasing $\langle\omega\rangle$, which contradicts the general expectation that inertial particles avoid regions of high vorticity. This trend is less apparent for the saddle region. At the duct center, variation in vorticity is small and hence the trend is not clear. This is expected since the duct center is a region of low shear. From the above discussion, it is clear that vorticity is not a good measure of preferential concentration of particles, especially in high shear regions.

The above trends are reflected in the PDFs of ω as well. Shown in Figs. 13–16 are the PDFs of ω for the four cross-sectional locations. It is clear that the most inertial ($\tau_p^+ = 8$) particles accumulate in regions of higher vorticity than the other particles, especially in the near-wall region (Fig. 13). In fact, they accumulate in regions of higher vorticity than even the fluid particles, shown in Fig. 12. As we move away from the wall, the PDFs of the less inertial particles are shifted to values of lower vorticity than the fluid PDF, indicating that the smaller particles accumulate preferentially in low vorticity regions. The above trends get weaker as one moves towards the duct center.

3.2. Effect of swirling strength

It is expected that particles will accumulate in regions of low swirling strength, λ_i. Swirling strength is defined as the magnitude of the imaginary part of the complex conjugate eigenvalues of the velocity gradient tensor. Ferry and Balachandar (2001) have shown that for a channel flow, particles collect in regions of low swirling strength. Unlike $\langle\omega\rangle$, $\langle\lambda_i\rangle$ accounts only for regions of

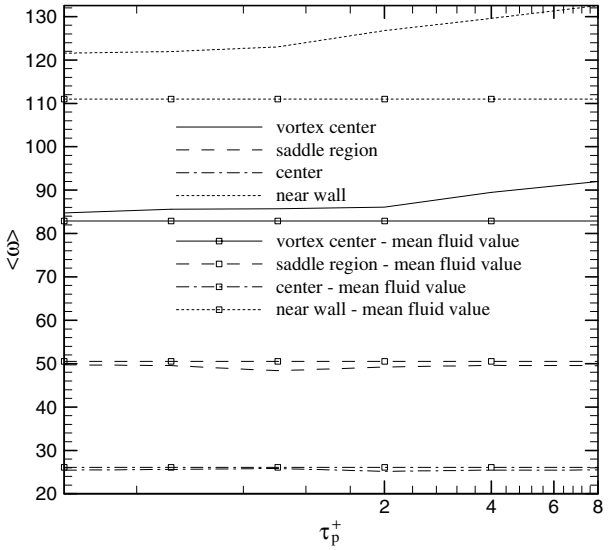

Fig. 12. Mean values of ω.

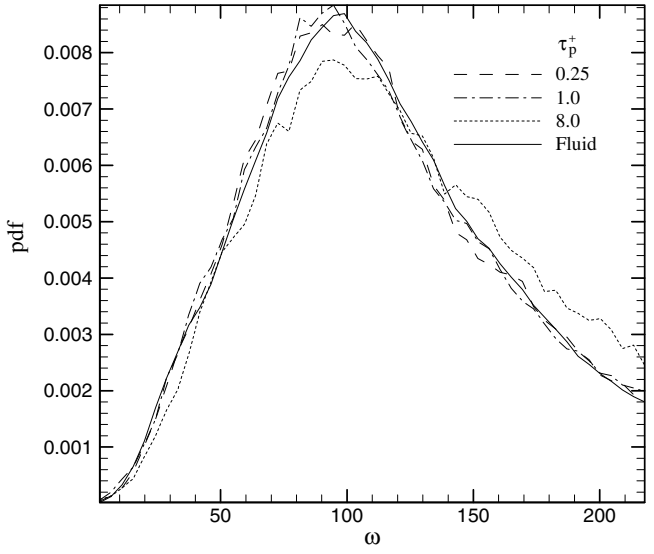

Fig. 13. PDFs of ω in the near wall region ($x^+ = 177.2$, $y^+ = 19.8$).

vorticity which have the nature of a core (Adrian et al., 2001). Therefore, it is expected that $\langle \lambda_i \rangle$ will be a more appropriate measure of preferential concentration in regions of flow with high shear. Shown in Fig. 17 is the variation of $\langle \lambda_i \rangle$ with τ_p^+ for the various cross-sectional locations, along with the mean values for the fluid particles. Firstly, particles of all response times studied accumulate in regions of lower $\langle \lambda_i \rangle$ when compared to the fluid particles. This trend was not as

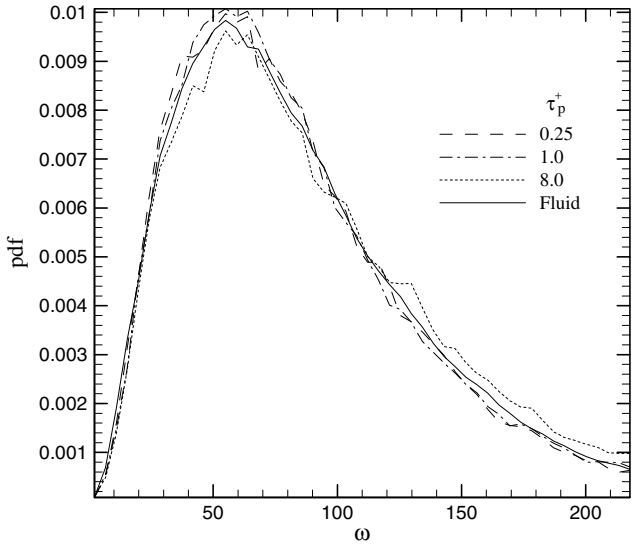

Fig. 14. PDFs of ω in the vortex center region ($x^+ = 76.7$, $y^+ = 31.2$).

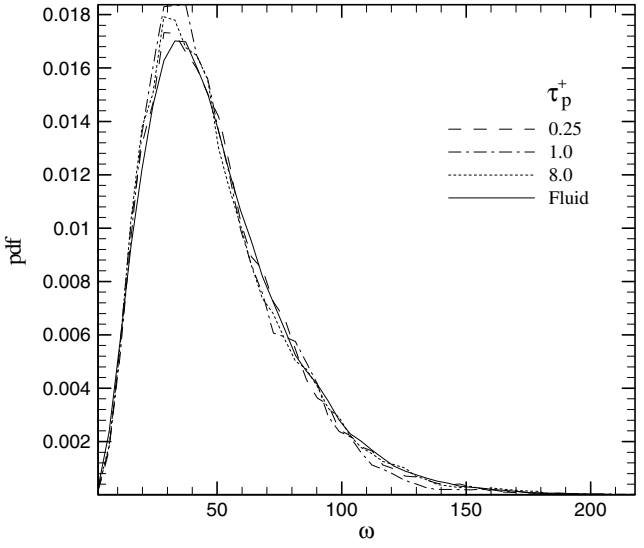

Fig. 15. PDFs of ω in the saddle region ($x^+ = 59.5$, $y^+ = 59.5$).

apparent in the case of vorticity magnitude. It is seen that for the near-wall and vortex center locations, as τ_p^+ increases particles accumulate in regions of decreasing $\langle \lambda_i \rangle$ before passing through a minimum around $\tau_p^+ = 4$. These trends in the mean values confirm the trends in channel flow study by Ferry and Balachandar (2001). The reversal in trend for the high inertia particles is to be expected as these particles do not respond to the surrounding fluid as well as the low inertia particles do. Hence, they do not show particular abhorrence for high swirling strength regions. As

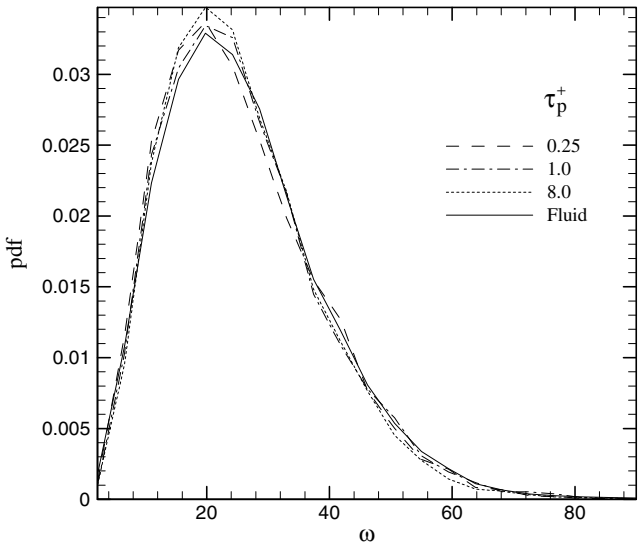

Fig. 16. PDFs of ω in the duct center region ($x^+ = 177.2$, $y^+ = 177.2$).

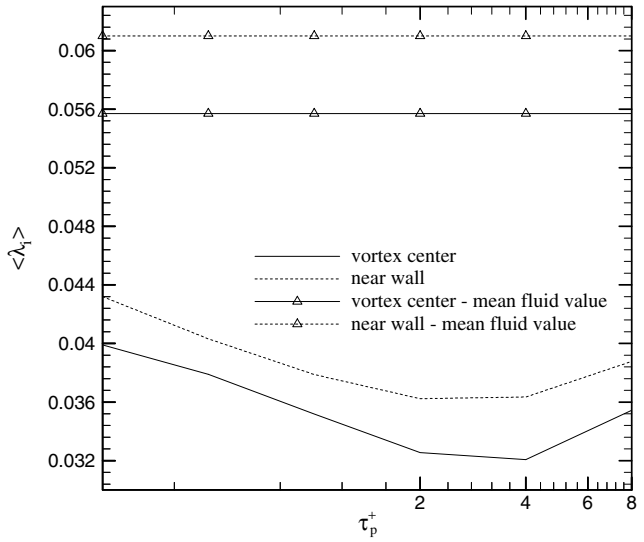

Fig. 17. Mean values of λ_i.

the distance from the wall increases, the swirling strength decreases. For the saddle region and the duct center (not shown), it is seen that the trends in $\langle\lambda_i\rangle$ with τ_p^+ are less apparent.

The PDFs of swirling strength for the near wall and vortex center regions are shown in Figs. 18 and 19. It is again clear that inertial particles accumulate in regions of smaller swirl compared to the fluid particles. Further, we can see that the smaller particles accumulate in regions of higher swirling strength compared to the large particles. As the distance from the wall increases, we see similar trends but to a lesser degree (figures not shown).

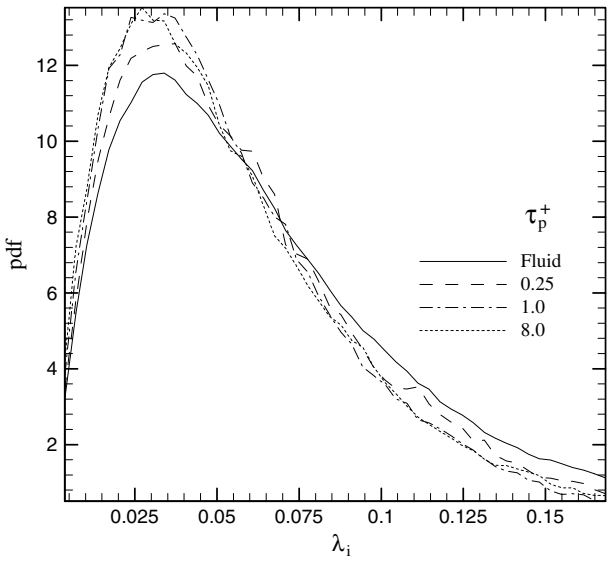

Fig. 18. PDFs of λ_i in the near wall region ($x^+ = 177.2$, $y^+ = 19.8$).

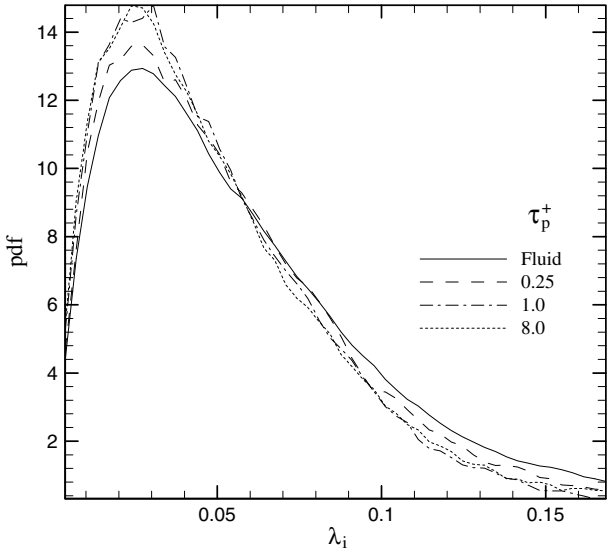

Fig. 19. PDFs of λ_i in the vortex center region ($x^+ = 76.7$, $y^+ = 31.2$).

3.3. Effect of maximum compressional strain-rate

It is now well known that particle collect in regions of high strain-rate (Squires and Eaton, 1990; Wang and Maxey, 1993). Ferry and Balachandar (2001) have shown that the maximum compressional strain-rate, σ_u, is a good measure of preferential concentration in a channel flow. It

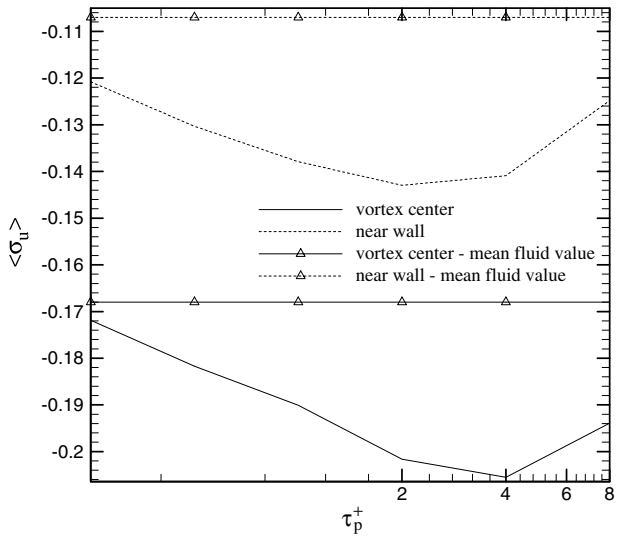

Fig. 20. Mean values of σ_u.

is defined as the most negative eigenvalue of the strain-rate tensor. Shown in Fig. 20 is the variation of $\langle\sigma_u\rangle$ with τ_p^+. It is seen that as τ_p^+ increases particles accumulate in regions of higher magnitudes of $\langle\sigma_u\rangle$ up to a certain τ_p^+, after which the trend is reversed. This maximum occurs in the range $2 \leqslant \tau_p^+ \leqslant 4$. The inertial particles experience higher magnitudes of $\langle\sigma_u\rangle$ than the fluid particles, indicating their preferential accumulation in regions of high strain. The trends for the other two locations are weak and are not shown.

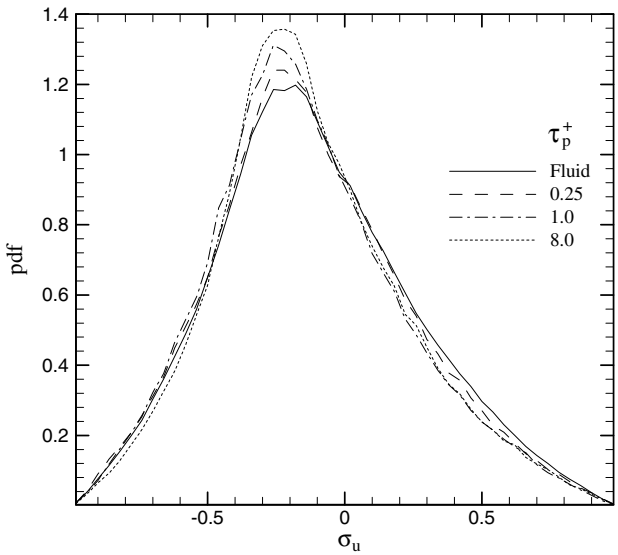

Fig. 21. PDFs of σ_u in the near wall region ($x^+ = 177.2$, $y^+ = 19.8$).

From the PDFs also, it can be seen that particles tend to collect in regions of higher compressional strain (negative strain) when compared to the fluid particles (see Figs. 21 and 22).

3.4. *Effect of* $\nabla\mathbf{u} : \nabla\mathbf{u}$

The final quantity we examine is $\nabla\mathbf{u} : \nabla\mathbf{u}$, which can also be expressed as $|\mathbf{S}|^2 - |\mathbf{\Omega}|^2$, where $\mathbf{S}$ and $\mathbf{\Omega}$ are the strain-rate and rotation-rate components, respectively, of the velocity gradient tensor. As mentioned earlier, positive values of $\nabla\mathbf{u} : \nabla\mathbf{u}$ indicate an accumulation of particles. Shown in Fig. 23 is the variation of $\langle\nabla\mathbf{u} : \nabla\mathbf{u}\rangle$ with τ_p^+. It is seen that for the near-wall and vortex center locations, as τ_p^+ increases particles accumulate in regions of increasing $\langle\nabla\mathbf{u} : \nabla\mathbf{u}\rangle$ before passing through a maximum. This maximum occurs within the range $2 \leqslant \tau_p^+ \leqslant 4$. These trends are similar to those seen in the channel flow work of Ferry and Balachandar (2001). Initially, with increasing inertia, particles show a greater affinity for regions of high $\langle\nabla\mathbf{u} : \nabla\mathbf{u}\rangle$. However, beyond a certain response time where the peak occurs, the particles are too inertial to respond to the surrounding fluid and hence the decrease in preferential accumulation. In the near wall region, particles have the maximum preferential concentration, when compared to other locations, indicated by the largest values of $\langle\nabla\mathbf{u} : \nabla\mathbf{u}\rangle$. Near the wall, the fluid velocity gradients are greater than away from the wall and hence the larger values of $\langle\nabla\mathbf{u} : \nabla\mathbf{u}\rangle$.

Figs. 24 and 25 display the PDFs of $\langle\nabla\mathbf{u} : \nabla\mathbf{u}\rangle$ in the near-wall and vortex center regions for three particle response times along with the fluid PDF. It is clear that $\nabla\mathbf{u} : \nabla\mathbf{u}$ measured at the particle locations is shifted towards a positive mean when compared to the mean value for the fluid particles (which is zero). The mean value increases initially with response time and decreases thereafter, reflecting the above trends.

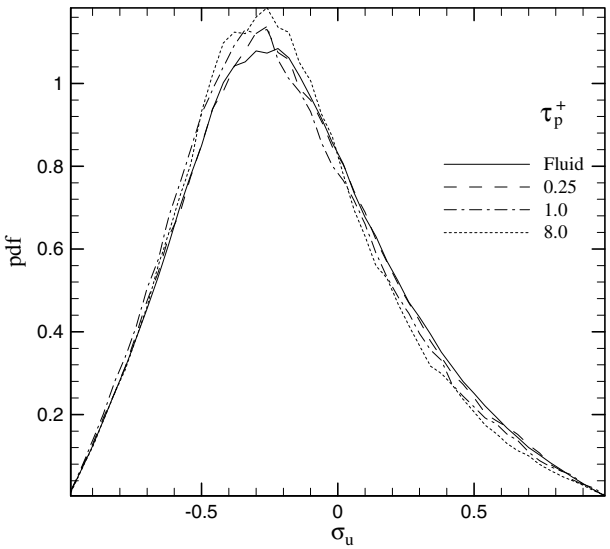

Fig. 22. PDFs of σ_u in the vortex center region ($x^+ = 76.7$, $y^+ = 31.2$).

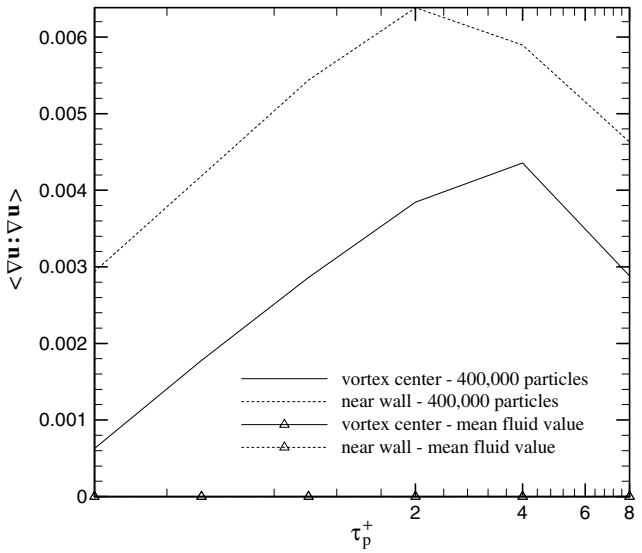

Fig. 23. Mean values of $\nabla \mathbf{u} : \nabla \mathbf{u}$.

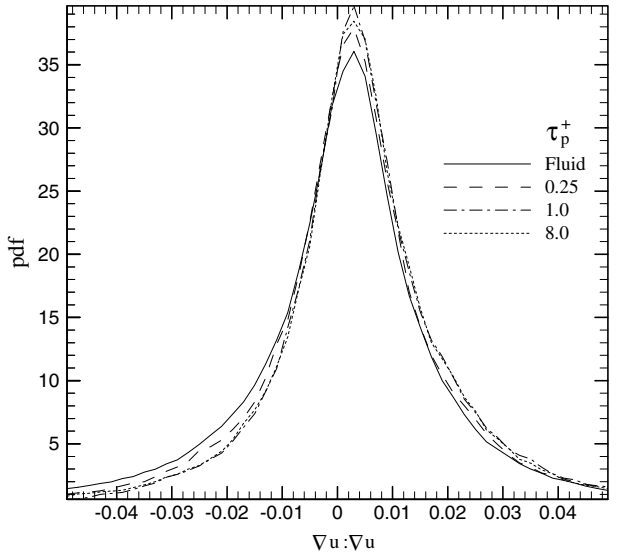

Fig. 24. PDFs of $\nabla \mathbf{u} : \nabla \mathbf{u}$ in the near wall region ($x^+ = 177.2$, $y^+ = 19.8$).

4. Conclusions

The preferential concentration of heavy particles in a turbulent square duct flow was studied using large eddy simulations. A dynamic subgrid kinetic energy model was used to model the

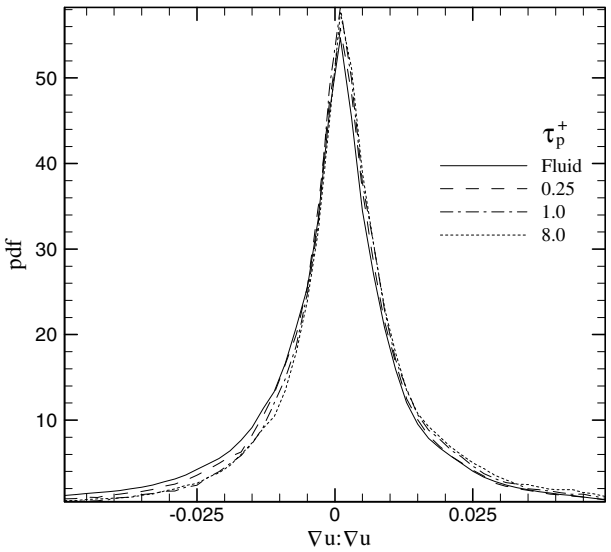

Fig. 25. PDFs of $\nabla\mathbf{u} : \nabla\mathbf{u}$ in the vortex center region ($x^+ = 76.7$, $y^+ = 31.2$).

unresolved scales. Six particle classes ($\tau_p^+ = 0.25$, 0.5, 1, 2, 4, and 8) and four cross-sectional locations were examined. Particles are seen to accumulate in regions of high $\nabla\mathbf{u} : \nabla\mathbf{u}$ and compressional strain and regions of low swirling strength. These trends are more pronounced for particles with intermediate response times. Of the four locations studied, preferential accumulation was most pronounced in the near-wall and vortex center regions. The duct center, being the farthest location from the walls, showed relatively weak preferential accumulation of particles.

Further, we have demonstrated that vorticity is not a precise measure of preferential concentration of particles, especially near the wall where shear dominates swirl. Swirling strength is a more appropriate measure of preferential concentration in regions of high shear.

Acknowledgements

The financial support provided by the Air Conditioning and Refrigeration Center and the Center for Simulation of Advanced Rockets (funded by the US Department of Energy through the University of California, under Subcontract number B341494) at the University of Illinois are gratefully acknowledged.

References

Adrian, R.J., Balachandar, S., Liu, Z.C., 2001. Spanwise growth of vortex structure in wall turbulence. Korean Soc. Mech. Engineers Int. J. 15, 1741–1749.

Bradshaw, P., 1987. Turbulent secondary flows. Ann. Rev. Fluid Mech. 19, 53–74.

Chung, J.N., Troutt, T.R., 1988. Simulation of particle dispersion in an axisymmetric jet. J. Fluid Mech. 186, 199–222.

Crowe, C.T., Troutt, T.R., Chung, J.N., Davis, R.W., Moore, E.F., 1995. A turbulent flow without particle mixing. Aerosol Sci. Tech. 22, 135–138.

Demuren, A.O., Rodi, W., 1984. Calculation of turbulence-driven secondary motion in non-circular ducts. J. Fluid Mech. 140, 189–222.

Druzhinin, O.A., Elghobashi, S., 1998. Direct numerical simulations of bubble-laden turbulent flows using the two-fluid formulation. Phys. Fluids 10, 685–697.

Eggels, J.G.M., Unger, F., Weiss, M.H., Westerweel, J., Adrian, R.J., Friedrich, R., Nieuwstadt, F.T.M., 1994. Fully developed turbulent pipe flow: a comparison between direct numerical simulation and experiment. J. Fluid Mech. 162, 175–209.

Ferry, J., Balachandar, S., 2001. A fast eulerian method for disperse two-phase flow. Int. J. Multiphase Flow 27, 1199–1226.

Fessler, J.R., Kulick, J.D., Eaton, J.K., 1994. Preferential concentration of heavy particles in a turbulent channel flow. Phys. Fluids 6, 3742–3749.

Gavrilakis, S., 1992. Numerical simulation of low-Reynolds-number turbulent flow through a straight square duct. J. Fluid Mech. 244, 101–129.

Horiuti, K., 1985. Large eddy simulation of turbulent channel flow by one-equation modeling. J. Phys. Soc. Jpn. 54, 2855–2865.

Huser, A., Biringen, S., 1993. Direct numerical simulation of turbulent flow in a square duct. J. Fluid Mech. 257, 65–95.

Kajishima, T., Miyake, Y., 1992. A discussion on eddy viscosity models on the basis of the large eddy simulation of turbulent flow in a square duct. Comput. Fluids 21, 151–161.

Kim, J., Moin, P., Moser, R., 1987. Turbulent statistics in fully developed channel flow at low Reynolds number. J. Fluid Mech. 177, 133–166.

Kim, W.W., Menon, S., Application of the Localized Dynamic Subgrid-Scale Model to Turbulent Wall-Bounded Flows. AIAA 97-0210, 1997.

Lazaro, B.J., Lasheras, J.C., 1992a. Particle dispersion in the developing free shear layer. Part 1. Unforced flow. J. Fluid Mech. 235, 143–178.

Lazaro, B.J., Lasheras, J.C., 1992b. Particle dispersion in the developing free shear layer. Part 2. Forced flow. J. Fluid Mech. 235, 179–221.

Lilly, D.K., 1992. A proposed modification of the germano subgrid-scale closure model. Phys. Fluids 4, 633–635.

Longmire, E.K., Eaton, J.K., 1992. Structure of a particle-laden round jet. J. Fluid Mech. 236, 217–257.

Loth, E., 2000. Numerical approaches for motion of dispersed particles, droplets and bubbles. Progr. Energy Combust. Sci. 26, 161–223.

Madabhushi, R.K., 1993. Direct and Large Eddy Simulation of Turbulent Flow in a Square Duct, Thesis, Dept. of Mech. Eng., Univ. of Illinois at Urbana-Champaign.

Madabhushi, R.K., Vanka, S.P., 1991. Large eddy simulation of turbulence-driven secondary flow in a square duct. Phys. Fluids 3, 2734–2745.

Madabhushi, R.K., Vanka, S.P., 1993. Direct numerical simulations of turbulent flow in a square duct at low Reynolds number. In: So, R.M.C., Speziale, C.G., Launder, B.E. (Eds.), Near-Wall Turbulent Flows. Elsevier, pp. 297–306.

Maxey, M.R., 1987. The gravitational settling of aerosol particles in homogeneous turbulence and random flow fields. J. Fluid Mech. 174, 441–465.

Meneveau, C., Katz, J., 2000. Scale-invariance and turbulence models for large-eddy simulation. Ann. Rev. Fluid Mech. 32, 1–32.

Squires, K.D., Eaton, J.K., 1990. Preferential concentration of particles by turbulence. Phys. Fluids 3, 1169–1178.

Tageldin, M.S., Cetegen, B.M., 1997. Development of mixing and dispersion in an isothermal droplet-laden, confined turbulent mixing layer. Combust. Sci. Tech. 130, 131–169.

Uijttewaal, W.S.J., Oliemans, R.V.A., 1996. Particle dispersion and deposition in direct numerical and large eddy simulations of vertical pipe flows. Phys. Fluids 8, 2590–2604.

Wang, Q., Maxey, M.R., 1993. Settling velocity and concentration distribution of heavy particles in homogeneous isotropic turbulence. J. Fluid Mech. 256, 27–68.

Wang, Q., Squires, K.D., 1996. Large eddy simulation of particle-laden turbulent channel flow. Phys. Fluids 8, 1207–1223.

Yeung, P.K., Pope, S.B., 1989. Lagrangian statistics from direct numerical simulations of isotropic turbulence. J. Fluid Mech. 207, 531–586.

Zhang, H., Ahmadi, G., 2000. Aerosol particle transport and deposition in vertical and horizontal turbulent duct flow. J. Fluid Mech. 406, 55–80.

Zhou, J., Adrian, R.J., Balachandar, S., Kendall, T.M., 1998. Mechanisms for generating coherent packets of hairpin vortices in channel flow. J. Fluid Mech. 387, 353–396.